

3D flow topology behind an aortic valve prosthesis

David Hasler^{1,*}, Dominik Obrist¹

1: ARTORG Center for Biomedical Engineering, University of Bern, Bern, Switzerland

* Correspondent author: email@adress.xxx.yz

Keywords: Tomographic PIV, Heart Valve Prosthesis, Hemodynamics, Refraction index matching

ABSTRACT

We have developed a hydraulic flow loop to replicate the flow conditions in the human aortic root. The setup features a test cell with a silicone phantom of the aortic root together with an aortic valve bioprosthesis. We used a refraction index matched fluid and multi-view camera setup for recording of the pulsatile fluid flow within the silicone phantom. The fluid is seeded with fluorescent particles. Tomographic particle image velocimetry is used to measure the three-dimensional instantaneous velocity field at specific phases of the pulse. We present results of the instantaneous and the phase averaged velocity field past the bioprosthetic valve. Based on a Reynolds decomposition of the velocity field, the root-mean-square velocity fluctuation reveals regions of turbulent flow. A specific flow topology can be identified that is directly related to the design features of the valve. This footprint allows for a quantitative performance assessment of the valve.

1. Introduction

Generally aortic valve prostheses - surgical valves as well as transcatheter aortic valve implantations (TAVI) - provide satisfactory clinical results for patients with heart valve diseases. That is, patients show reduced pressure gradient across the valve prosthesis and have moderate aortic peak blood flow velocities after the intervention. From a clinician's point of view the hemodynamic condition has improved. Nonetheless, some issues with respect to the performance of the valve are not yet understood and post-operative complications (e.g. immobilized valve leaflets, stroke and coronary disease) can occur. The reasons are multifactorial (Makkar et al 2015, Del Trigo et al 2015). On the other hand, high shear stresses at the wall of the aorta and in the bulk flow as well as flow stasis in high pressure zones are known to be responsible for blood damage (hemolysis) or thrombus formation and therefore significantly contribute to the risk of ischemia caused by obstruction of blood vessels. Both situations possibly occur after replacement of the aortic valve. Hence, an accurate understanding of the flow conditions in the aortic root is of central importance for assessing the performance of the prosthesis.

In the present study we investigate the three-dimensional flow topology past an aortic valve bioprosthesis (AVBP) under physiological flow conditions. Besides the 3D velocity field and derived quantities (e.g. shear stresses, turbulent kinetic energy (TKE)), also functional relations are of interest: how are the kinematics of the valve influenced by specific flow structures? How is the flow field affected by an immobile valve leaflet or a suboptimal deployment of the valve? Etc.

Bioprosthetic valves are fabricated from biological tissue (e.g. bovine pericardium) and their design is motivated by the anatomy of native aortic valves with three cusps. In contrast to mechanical valves with restricted degrees of freedom, the leaflet kinematics of bioprosthetic valves are smoother but more complex. Moreover, the biomimetic design of bioprosthetic valves leads to blood flow which is similar to the physiological flow in native valves. This helps to mitigate the risk of blood trauma associated with non-physiological flow due to sharp edges, small orifices or abrupt valve kinematics. At the same time, the flow field past an AVBP is inherently three-dimensional typically without any levels of symmetry.

For the investigation of the three-dimensional flow field we used a tomographic particle imaging velocimetry (tomo-PIV) system (FlowMaster, LaVision, Göttingen, Germany) and a physiological flow model, replicating the flow conditions in the aortic root. In the past years, tomo-PIV (Elsinga et al 2006) has been used for studying flows of various complexity, e.g. free-shear flows (Violato and Scarano 2011, Scarano and Poelma 2009), boundary layer flows (Atkinson et al 2010). Buchmann (2011) used tomo-PIV to measure the flow in a silicone model of the carotid artery and compared the results with stereo PIV measurements. Scarano (2012) outlined the main principles and challenges of tomo-PIV and some tomo-PIV applications are reviewed. In a recent study (Hasler et al. 2016), the authors presented the results of the 3D flow field past an AVBP for steady and pulsatile (but non-physiological) flow conditions. In the present work, we used the tomo-PIV system together with an in-vitro flow replicator which simulates the flow conditions in a human aortic root.

2. Method

2.1 Physiological Flow Model

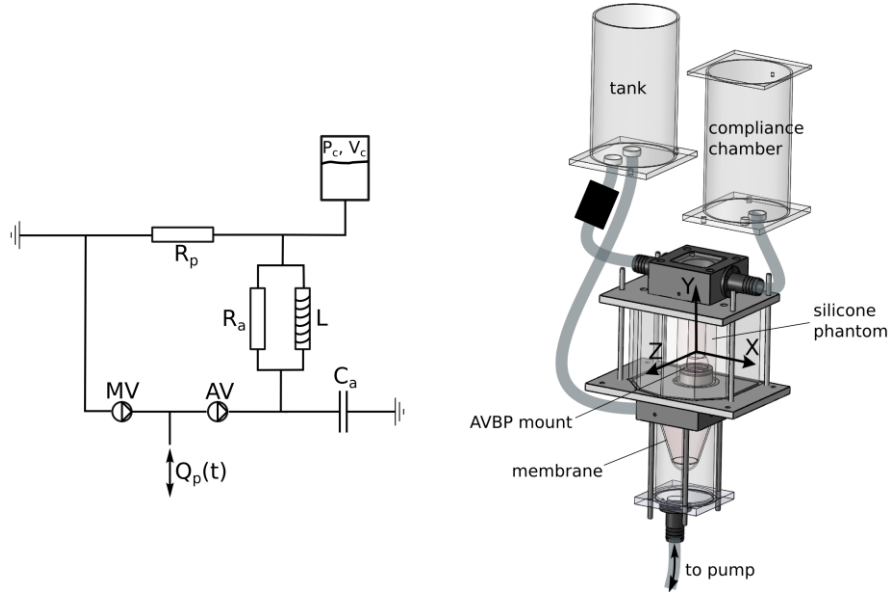


Fig. 1 Right: Schematic of the test cell with the silicone phantom inside and several parts of the flow loop. Left: Lumped parameter model of the flow loop, where MV and AV represent the mitral and the aortic valve, respectively, R_a and R_p represent the arterial and the peripheral resistance, L models the inertia of the fluid, C_a is the compliance of the silicone phantom, P_c and V_c are the pressure and the volume in the compliance chamber and Q_p is the flow rate provided by the pump.

A *Carpentier Edwards Model 2625 Aortic valve* (Edwards Lifesciences, Irvine, USA) is inserted in a transparent silicone phantom (ELASTOSIL 601, Wacker Silicones, Germany) of the aortic root. The simplified geometry is a combination of the data given in Swanson and Clark (1974) and a straight tube. The silicone phantom is integrated in a cell with a transparent housing offering four windows with a 30 degree angle between the surface normal for optical access for image recording. Figure 1 shows the test cell with the silicone phantom inside. Fluid seeded with fluorescent particles flows inside the phantom. The same fluid without particles fills the gap between the phantom and the housing. Optical distortions within the test-cell are minimized by matching the refraction index of the fluid and the silicone phantom. Figure 2 depicts silicone part (fabricated together with the silicone phantom) immersed in the test fluid. Furthermore the (apparent) kinematic viscosity of blood $\nu \approx 4 \text{ mm}^2/\text{s}$ is approximated with the test fluid. To this end, we used a water-glycerol-sodium chloride mixture (0.5/0.33/0.17 by weight respectively) yielding a dynamic viscosity of $\nu = 4.8 \text{ mm}^2/\text{s}$.

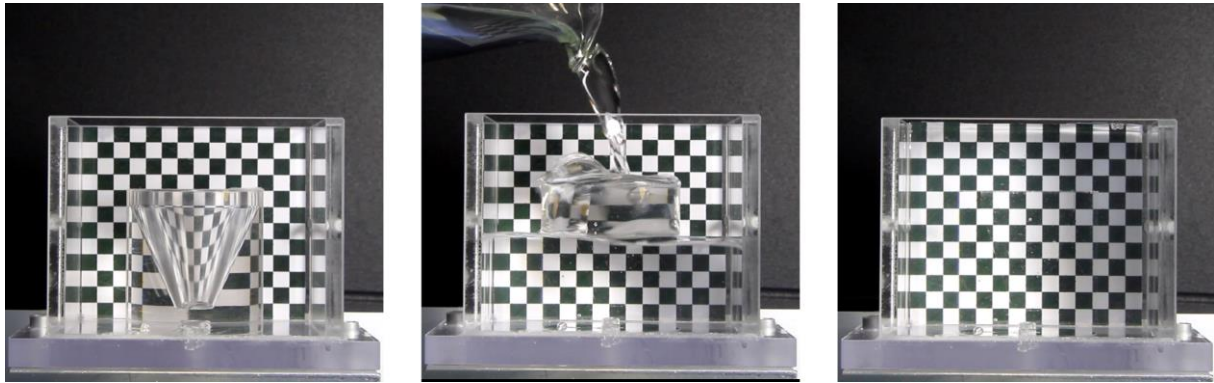


Fig. 2 Cone shaped silicone part to assess quality of refraction index matched fluid. First surrounded by air (left), during filling with the test fluid (middle) and completely immersed in the test fluid (right).

2.2 Test Cell

Fluid is driven through the flow loop by means of a membrane pump located at the bottom of the test cell mimicking the left ventricle. A piston pump is used for cyclic loading of the membrane. From the membrane chamber fluid is pumped through the silicone phantom passing the AVBP mounted on the bottom lid. At the top, the test cell is connected (T-junction) to an air chamber representing the total arterial compliance and a resistance element representing the peripheral resistance in the systemic circulation. After this resistance, fluid discharges into an open tank. The tank connects further to the membrane chamber where a second valve (representing the mitral valve) is mounted to assure unidirectional, circulatory flow. We used a lumped parameter model (Figure 1) for designing and dimensioning of the key elements in the flow loop (compliance chamber, resistance, piston profile) according to physiological data given in the literature (Stergiopoulos et al 1999).

2.3 Image Recording and Further Instrumentation

A two camera system is employed together with mirrors to record simultaneous images from four different angles. The lines of sight through the left and right pairs of neighboring windows are reflected with a specific mirror configuration (Figure 3) onto parallel lines of sight. By this, two CCD cameras (Imager LX, LaVision) record two different views on the left and right halves of the camera sensor. This composite camera image is subsequently treated as two images from separate cameras, providing effectively four images from different angles. In addition, the flow loop features two pressure sensors before and after the AVBP to measure the transvalvular pressure gradient.

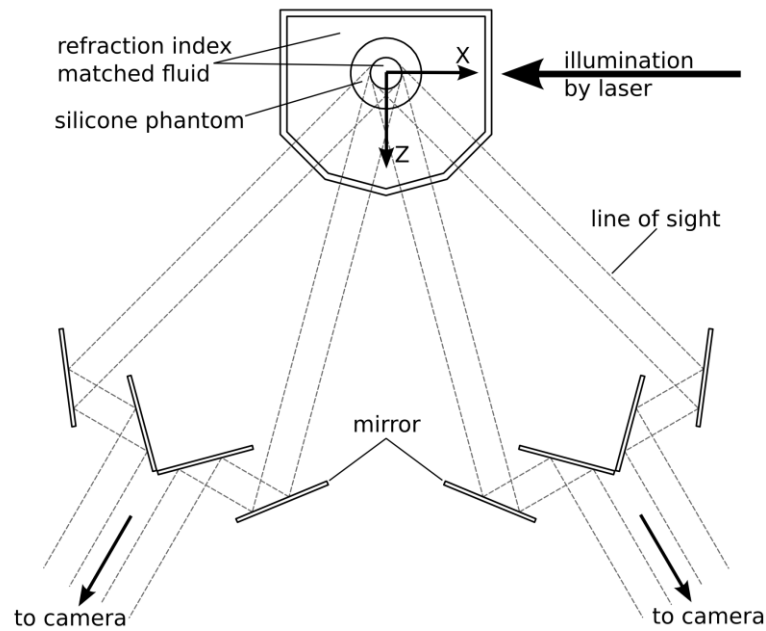


Fig. 3 Sketch of the test cell and the mirror configuration. Lines of sight with four distinct viewing angles are redirected onto two cameras.

2.4 Illumination

For volume illumination, a double-pulse Nd:YAG laser (Nano L PIV, Litron Lasers, Rugby, England; 532 nm; 235 mJ/pulse) is used together with volume optics. The direction of illumination is along the X-axis (Figure 3). The depth of the illumination volume is larger than maximum inner diameter of the phantom (> 34 mm).

2.5 Camera Calibration

A third order polynomial is used as model for the mapping of three-dimensional coordinates in the world reference frame $\{X, Y, Z\}$ to two-dimensional coordinates $\{x, y\}$ on the camera sensors. The test cell offers the possibility of replacing the silicone phantom with a calibration plate comprising an array of marks at precisely known locations at two different depths on the plane. After mounting of the calibration plate, the test cell is filled with index matched fluid. This produces an optical environment similar to final configuration with the silicone phantom with test fluid at the inside and outside.

2.6 Tomographic PIV

As a first step, the raw images are preprocessed applying a sliding minimum subtraction for background removal and a normalization step using a local average to reduce inhomogeneities due to uneven illumination. Moreover, a masking technique is used to reduce the image to the

part corresponding to the flow region inside the silicone phantom. Volume self-calibration (Wieneke 2008) is then applied using images of sparsely seeded flow. This effectively reduces mapping errors, e.g. due to remaining optical distortions at the fluid-silicone interface. The mapping accounts for various depths (Z-direction) in the measurement volume. Next, a multiplicative algebraic reconstruction technique (MART) is performed to generate a 3D voxel-based representation of the particle cloud within the silicon phantom. After reconstruction, a multistep 3D cross-correlation is performed to determine the 3D velocity field with a resolution of 0.65 mm. The parameters of the 3D cross-correlation used in the PIV computations are the same as in Hasler et al. (2016). More details about the tomo-PIV system in general are given in the same reference.

2.7 Experimental Protocol

We used a physiological flow profile where the systole and diastole account for 1/3 and 2/3 of the pulse, respectively. Figure 4 shows the flow rate induced by the pump $Q_p(t)$. For the nominal inner diameter of the silicone phantom of $d_a = 24$ mm, the mean (in cross-section) peak (in pulse) velocity in the measurement volume is $u_a = 0.7$ m/s. A period of $T = 1$ s was chosen yielding a heartrate of 60 beats per minute. For the resulting Reynolds number $Re = d_a u_a / \nu = 3500$ and Womersley number $\alpha = d_a \sqrt{2\pi / (T\nu)} = 27$ flow instabilities can be expected. Continuous acquisition of images yielded measurements of the instantaneous 3D velocity field $\vec{U}(\vec{X}, t) = [U_x(\vec{X}, t), U_y(\vec{X}, t), U_z(\vec{X}, t)]$, with $\vec{X} = [X, Y, Z]$, at a frequency of 3.1 Hz which is not sufficient to fully resolve \vec{U} in time. However, the flow field has essentially no memory of the preceding pulse, because we found that the flow in the test section comes to rest almost completely toward the end of the diastole. We therefore applied phase averaging for different phases $\phi_j = j 2\pi dt / T$, with $j = 0, 1, 2, \dots, 19$ and $dt = 0.03$ s. For each phase velocity fields from $N = 10$ subsequent pulses were measured, whereby the first image was recorded after 10 pulses from the onset of the pump due to an initial transient phase. From each set we calculate a phase averaged mean velocity field

$$\langle \vec{U}(\vec{X}, t_j) \rangle = \frac{1}{N} \sum_{k=1}^N \vec{U}(\vec{X}, t_j + kT), \quad \text{with} \quad t_j = T \frac{\phi_j}{2\pi}.$$

This allows a Reynolds decomposition of the instantaneous flow field,

$$\vec{U} = \langle \vec{U} \rangle + \vec{u}$$

where \vec{u} is the fluctuation of the velocity field. From this, the root-mean-square velocity fluctuation $u_{rms} = \langle \vec{u} \cdot \vec{u} \rangle^{1/2}$ is computed.

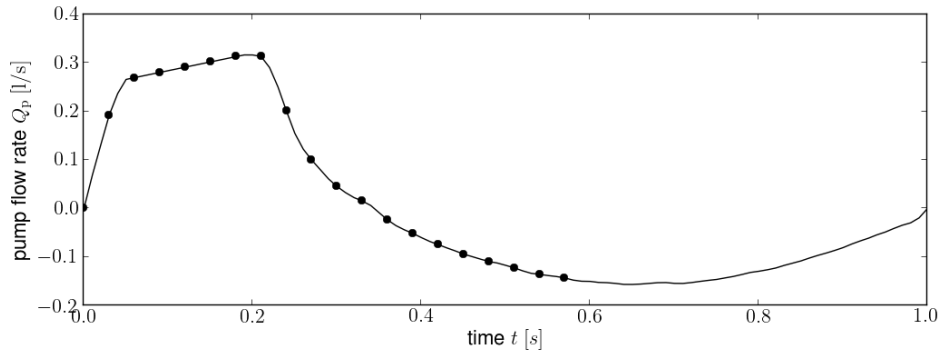


Fig. 4 Profile of the flow rate induced by the pump (solid line). For each instance of image acquisition (black dot) phase averaging was carried out.

3. Results

We present flow fields \vec{U} and $\langle \vec{U} \rangle$ for a single instance t_j (with $j = 5$) during the peak systolic phase of the pulse. Figure 5 depicts an instantaneous flow field taken from a set of $N = 10$. The valve is mounted 1 to 2 mm beneath the visualized data sets. Panel (b) on Figure 5 reveals a star-like flow topology which is especially pronounced close to the valve. This velocity profile is due to the particular shape of the valve orifice. A central jet with three adjacent lobes ejects through the leaflets of the valve. The fastest velocities (3.4 m/s) are found in the center of the jet and close to the valve. The lobes impinge on the phantom wall in the region of the sino-tubular junction (where the three aortic sinuses connect to the ascending aorta). The chosen interrogation window size is limited by the seeding density and suitable for velocities in the bulk. At the wall, the measurements presented here have a limited accuracy due to the high velocity gradients and also due to the bias error arising from cross-correlation across the fluid silicone interface. Nonetheless it can be expected that wall shear stresses are greatly increased in the regions where the high velocity lobes impinge on the wall.

In addition, three shear layers can be observed opposite to each lobe of the star-shaped jet. Correspondingly, panels (g) to (i) of Figure 5 show three zones of flow recirculation. Further downstream, the central jet and the three adjacent lobe separate, giving rise to additional shear layers. Approximately a distance d_a from the valve, the velocity profile starts to get irregular and smaller flow structures appear (see panels (b) and (d) in Figure 5).

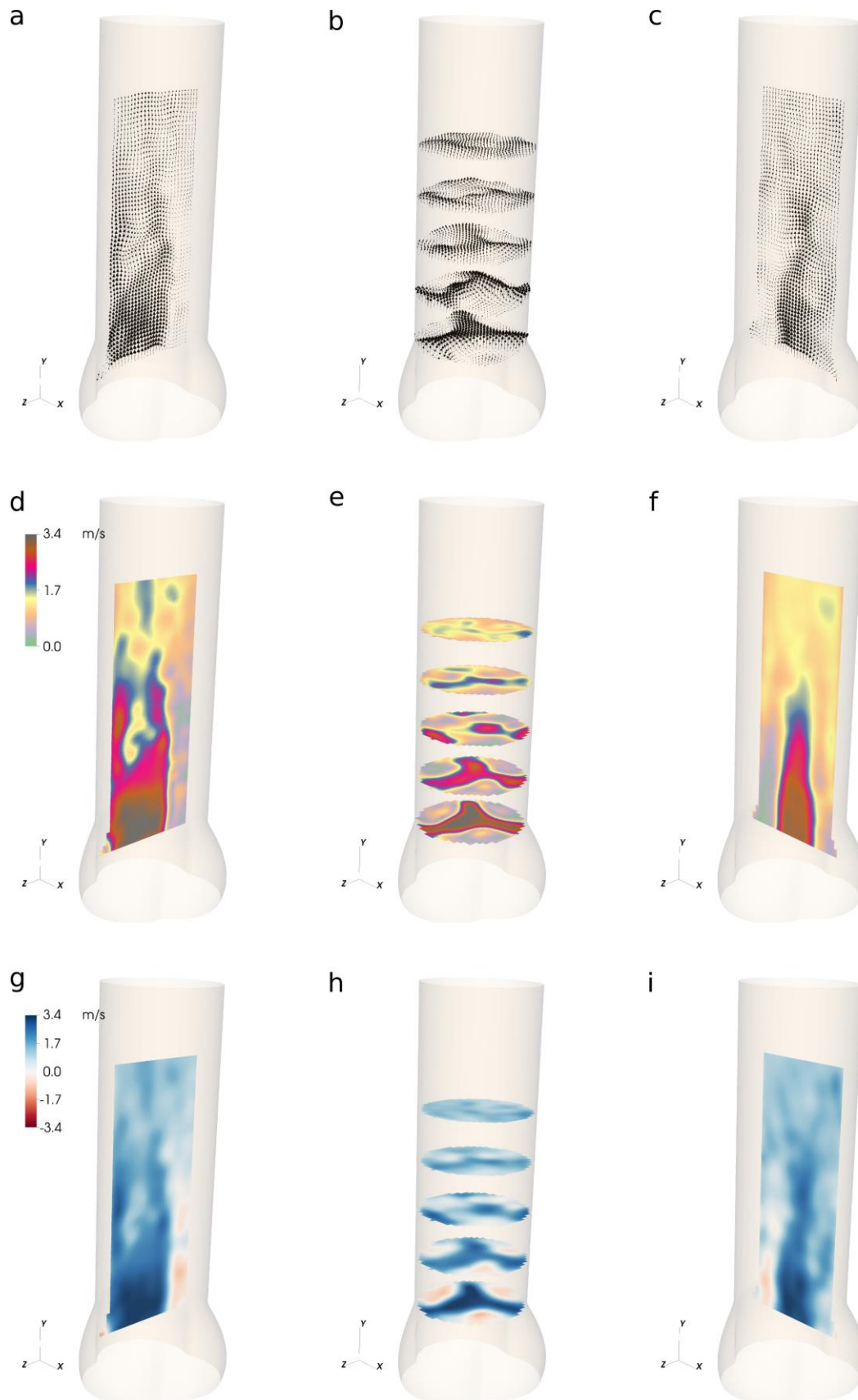


Fig. 5 Instantaneous flow field \vec{U} during peak systolic phase. Velocity vector field (a, b, c), and contour plots of the velocity magnitude (d, e, f) and the streamwise velocity component U_y .

In Figure 6 the mean flow field $\langle \vec{U} \rangle$ and the rms velocity fluctuation u_{rms} obtained from $N = 10$ instantaneous velocity fields are visualized. The magnitude of $\langle \vec{U} \rangle$ (Figure 6a,b,c) even more clearly depicts the star-shaped velocity profile. The similarities between $\langle \vec{U} \rangle$ and \vec{U} become weaker further away from the valve and the mentioned small scale structures average out on $\langle \vec{U} \rangle$. This can also be seen on panels (d), (e) and (f) in Figure 6 where strong velocity fluctuations appear after a certain distance from the valve. In addition, the three shear layers are concurrent with regions of distinctly increased u_{rms} , which can be explained by shear induced flow instabilities growing as they are advected downstream. The strongest velocity fluctuations appear at a distance d_a away from the valve and amount to approximately $1.5u_a$.

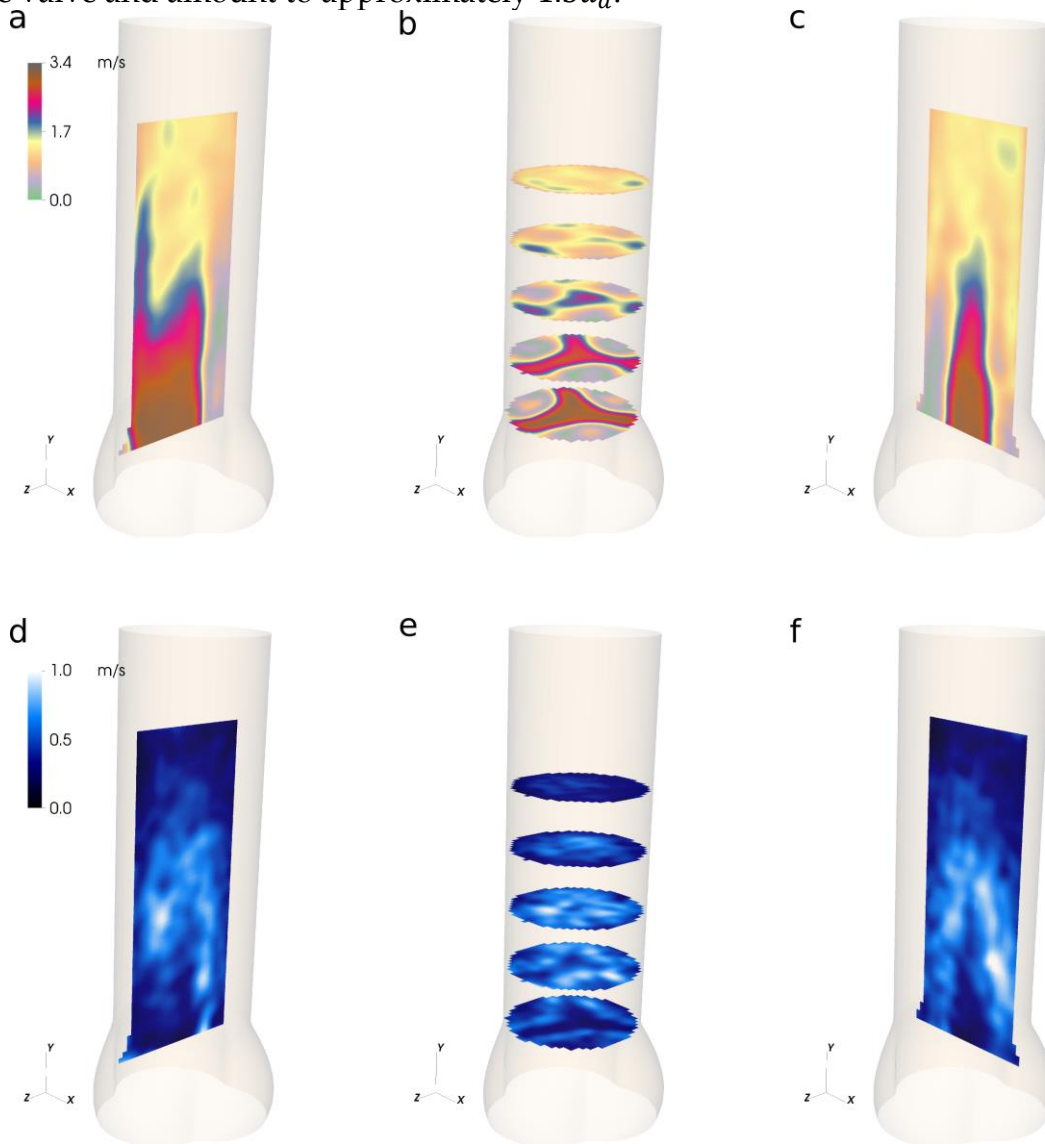


Fig. 6 Magnitude of the mean velocity field $\langle \vec{U} \rangle$ and rms velocity fluctuation u_{rms} for the same instance as in Figure 5.

4. Discussion

The pulsatile flow past a prosthetic (or native for that manner) aortic heart valve contains many interesting flow features: Asymmetric velocity profiles, vortex shedding, turbulent flow, flow stasis, bifurcations, etc. Tomo PIV measurements provide a great insight in this complex three-dimensional flow topology. The results presented here were conducted with an acquisition frequency equal to the frequency the pulsatile flow. Phase-averaging revealed the dynamic behavior of the mean flow. To reveal the full dynamic behavior of the flow, time-resolved tomo-PIV experiments with higher acquisition frequency have to be performed. The most prominent feature of the flow, the star-like jet, is most considerable at peak flow. In terms of heart valve hemodynamics, the star-like jet is unfavorable in several ways: The impingement at the wall causes high wall shear stress and potentially damages the endothelial layer. The accompanying recirculation and flow instabilities cause increased shear stresses and raise the pressure gradient in the aortic root. A circular orifice of the open valve is therefore beneficial with respect to its performance. The observed feature is likely specific for the type of aortic bioprosthesis that we used in our experiments. The fluid dynamic footprint of a different type of valve might have a different topology, with distinct but crucial features.

5. References

- Atkinson et al (2011) The accuracy of tomographic particle image velocimetry for measurements of a turbulent boundary layer. *Experiments in Fluids*, 50:1031-1056.
- Buchmann et al (2011) Tomographic particle image velocimetry investigation of the flow in a modeled human carotid artery bifurcation. *Experiments in Fluids*, 50:1131-1151.
- Del Trigo et al (2016) Incident, timing and predictors of valve hemodynamic deterioration after transcatheter Aortic valve replacement. *Journal of the American College of Cardiology*, 67(6):644-655.
- Elsinga et al (2006) Tomographic particle image velocimetry. *Experiments in Fluids*, 41 :933-947.
- Hasler D, Landolt A, Obrist D (2016) Tomographic PIV behind a prosthetic heart valve. *Experiments in Fluids*, 57(5):1-13.
- Makkar et al. (2015) Possible subclinical leaflet thrombosis in bioprosthetic aortic valves. *New England Journal of Medicine*, 373(21):2015-2024.
- Scarano F (2012) Tomographic PIV: Principles and practice. *Measurement Science and Technology*, 24:012001.
- Scarano F and Poelma C (2009) Three-dimensional vorticity patterns of cylinder wakes. *Experiments in Fluids*, 47:69-83.
- Stergiopulos N, Westerhof BE, Westerhof N (1999) Total arterial inertance as the fourth element of the windkessel model. *American Journal of Physiology* 276:H81-H88.
- Swanson WM and Clark RE (1974) Dimensions and Geometric Relationships of the human aortic valve as a function of pressure. *Circulation Research*, 35(6):871-882
- Violato D and Scarano F (2011) Three-dimensional evolution of flow structures in transitional circular and chevron jets. *Physics of Fluids*, 23
- Wieneke B (2008) Volume self-calibration for 3D particle image velocimetry. *Experiments in Fluids*, 45:549-556